Technical Memo

ECMWF
European Centre for Medium-Range Weather Forecasts

920

Solar eclipses in the IFS

Philippe Lopez
(Research Department)

December 2024

Series: ECMWF technical memoranda

A full list of ECMWF Publications can be found on our web site under:
http://www.ecmwf.int/en/publications/

Contact: library@ecmwf.int

European Centre for Medium Range Weather Forecasts, Shinfield Park, Reading, RG2 9AX, UK

Abstract

Until now, ECMWF's Integrated Forecasting System (IFS) was not able to represent the meteorological consequences of the strong reduction in incoming solar radiation associated with occasional solar eclipses. Therefore, developments have been made in the IFS to include the effects of solar eclipses in both operational weather forecasts and data assimilation (from IFS cycle 50R1 onwards), as well as in ECMWF's future reanalysis ERA6 (to be based on IFS cycle 49R2). As illustrated for the recent total solar eclipse of 8 April 2024 over North America, the inclusion of such event in IFS forecasts has a significant and widespread impact on low-level tropospheric temperature, humidity and wind over land, as well as on temperature in the stratospheric ozone layer. Consistent with previous studies based on observations and numerical simulations, the strongest impacts are found over land regions with a stable planetary boundary layer and clear-sky conditions. The drop in predicted 2-m temperature reaches 7°C inside the band of totality, while a persistent cooling in excess of 1°C affects most of North America, even several hours after the eclipse. These simulated impacts are successfully validated using high temporal frequency ground-based observations provided by the Purdue University in Indiana (USA). It is also demonstrated that including solar eclipses in ECMWF's 4D-Var data assimilation system helps to reduce background departures over the whole region affected by the eclipse, especially for temperature in the low troposphere and in the stratosphere. This, in turn, can increase the number of effectively assimilated observations by several percents. Furthermore, even bigger benefits are expected when satellite solar reflectances start to be assimilated in the IFS. Even though these developments are not likely to noticeably improve the overall performance of the IFS, they should significantly improve both analyses and forecasts during the two to five eclipse days that occur every year.

Plain Language Summary

ECMWF's forecasting system has been modified to include the effects of the two to five solar eclipses that affect our planet every year. As illustrated here for the recent total solar eclipse of 8 April 2024 over North America, the comparison of two numerical weather forecasts, with and without eclipse, shows that the atmosphere just above ground usually becomes much cooler, moister and quieter (weaker winds) when sunlight vanishes, even in regions where the sun is only partially eclipsed. These effects are successfully verified using dedicated measurements from ground-based weather stations in Indiana (from Purdue University, USA), and they also agree with other studies. In the forecast, the ozone layer in the upper atmosphere also gets cooler when the eclipse occurs, due to the drop in solar radiation. Besides, including solar eclipses is also beneficial when generating initial conditions for weather forecasts using observations, since the model agrees better with observations, right from the start. This also means that more observations can be successfully taken into account, which can further improve initial conditions and possibly weather predictions run from the latter.

1 Introduction

Between two and five times a year, our planet is affected by a solar eclipse (either total, annular or partial). Figure 1 gives a simple reminder of the main mechanism of a solar eclipse, including the definition of the penumbra (partial eclipse) and umbra (total eclipse). Whether the cone of the umbra reaches or not the surface of the Earth depends on the relative distances of Sun and Moon to our planet. A solar eclipse causes a drop in incoming solar radiation over an area covering up to a fourth of the Earth and for up to 6 hours (from the first to the last contact of the lunar penumbra with the Earth's surface). In the case of a total eclipse, direct solar radiation may completely vanish for up to 7.5 minutes at any given location on the central line of totality, while the partial phase typically lasts for around 2.5 hours. Until

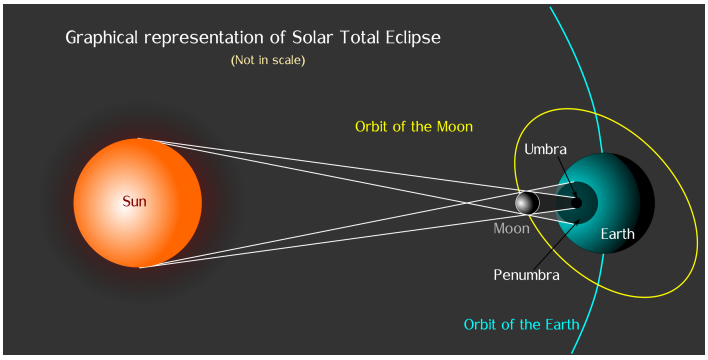

Figure 1: Solar eclipse schematic, showing the definition of the penumbra and umbra. Original figure from Sanu N., CC BY-SA 4.0 https://creativecommons.org/licenses/by-sa/4.0, via Wikimedia Commons.

now, solar eclipses have been neglected in ECMWF[1]'s Integrated Forecasting System (IFS). However, even though long-term forecast scores are expected to be largely unaffected by that absence, previous studies based on observations and numerical simulations (see the detailed reviews by Aplin *et al.*, 2016; Elmhamdi *et al.*, 2024) have shown that the meteorological impact can be significant on eclipse days, with, for instance, a possible low-level temperature drop of several degrees Celsius over land regions, the amplitude of which depends on local weather conditions and solar elevation. Other well-observed consequences include a frequent drop in low-level wind speed, together with occasional changes in wind direction, as well as a usual drying (resp. moistening) before (resp. after) eclipse maximum. Very recently, Pasken *et al.* (2024) reported on the effects of the total solar eclipse of 8 April 2024 on the weather over Missouri (USA), using observations from ground-based stations, radiosondes, as well as instrumented drones, with a particular interest in the time scales of the local changes observed during the eclipse. That particular eclipse was selected in the present work, for validation purposes.

This report explains how the prediction of solar eclipses has been included in the IFS and assesses the resulting meteorological impacts in both forecast and data assimilation. It should be stressed that the comparison of numerical weather forecasts with and without eclipse, as conducted in the present study, permits a unique evaluation of the impact of a given eclipse, which is not possible when working with observations alone, since the scenario without eclipse is obviously unknown in the real world.

First, section 2 provides references to the IFS, the forecasting and data assimilation system used in this work. Section 3 describes the reference data used for eclipse path validation, as well as the high-temporal frequency ground-based weather observations used for verifying IFS forecasts. Section 4 introduces the practical implementation of astronomical calculations in the model. Section 5 presents the impacts of the recent total solar eclipse of 8 April 2024 on the main meteorological variables in IFS forecasts, together with a verification against independent surface observations. For the same event, section 6 highlights the additional benefits of including solar eclipses in the data assimilation process, by which analyses (which serve as initial conditions to numerical weather forecasts) are produced. Summary and conclusions follow in section 7.

[1] European Centre for Medium-range Weather Forecasts

2 ECMWF's IFS

The IFS comprises a forecasting and a data assimilation components, detailed descriptions of which can be found at *https://www.ecmwf.int/en/publications/ifs-documentation* and in Courtier *et al.* (1994), respectively. The IFS uses a spectral representation for temperature, vorticity, divergence and surface pressure, while all other variables (e.g., specific humidity, hydrometeors, ozone) are treated in physical space (grid points). Operational weather forecasts (as of October 2024) are run at 9-km resolution and on 137 vertical model levels (top at 0.01 hPa), with a time step of 7.5 min.

The data assimilation system is based on the four-dimensional variational (4D-Var) method (Courtier *et al.*, 1994). During each 4D-Var assimilation cycle (typically every 6 hours), information coming from around 100 million observations (e.g., from polar-orbiting and geostationary satellites, radiosondes, aircraft, ground-based weather stations, ships, buoys and ground-based precipitation radars) is blended with a priori information coming from a previous short-range forecast (the *background* state) to produce the so-called *analysis*. The latter is expected to provide an optimal 3D representation of weather and surface conditions at a given time, which can serve as initial conditions in new weather forecasts. To perform the desired blending of information, the 4D-Var method, as implemented at ECMWF, currently relies on four iterative minimizations of the square distance between the unknown state (the future analysis) and both observations and model background state, weighted by their assumed respective errors. The relative magnitudes of these errors determine whether the final analysis is closer to the observations or to the background state. In ECMWF's operations, the four 4D-Var minimizations are performed at increasing resolutions of 80, 62, 50 and 39 km. 4D-Var trajectories, which are used to compute observation−model departures and serve as reference states in the linearized version of the forecast model, are run at 9-km resolution.

3 Validation data

3.1 Eclipse path reference data

Total eclipse central path locations computed with high accuracy by Fred Espenak (NASA/GSFC[2], Emeritus) and available at *https://eclipse.gsfc.nasa.gov/solar.html* were taken as a reference for validating IFS predicted paths over the period 1900 to 2100.

3.2 Meteorological observations

High temporal frequency meteorological observations were needed for properly validating IFS forecasts during the fast-evolving conditions induced by the solar eclipse of 8 April 2024, the focus of the present work. Traditional SYNOP (ground-based synoptic station) or METAR (airport-based) data were deemed unsuitable for eclipse weather verification, due to their relatively coarse temporal sampling (half-hourly at best). Besides, radiosonde data from the national US network were not available during the period close to eclipse maximum. Luckily however, 3-second measurements from three Purdue University's Mesonet weather stations located near or inside the path of totality over Indiana (USA) could be used in this study (see Table 1).

[2]National Aeronautics and Space Administration/Goddard Space Flight Center

Station name	Altitude [m]	Longitude [°]	Latitude [°]
Shawnee Hills Farm Research Station	210	−86.784	38.956
Asel Family Farm	295	−85.150	40.255
Davies Agricultural Center	225	−86.463	41.311

Table 1: Information about the selected Purdue Mesonet stations in Indiana (USA).

From this data set available at *https://ag.purdue.edu/indiana-state-climate/purdue-mesonet/2024-solar-eclipse/*, measurements of air temperature at four heights (namely 0.5, 1.5, 2 and 3 m), 2-m dew point temperature, 3-m wind speed and surface solar flux have been used in this work. Figure 2 shows an example of the typical instrumentation at a Purdue Mesonet station.

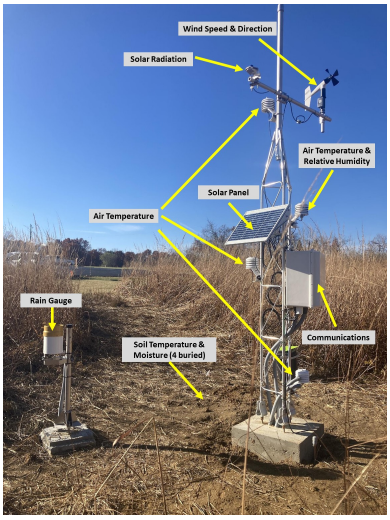

Figure 2: Example of the typical instrumentation at a Purdue Mesonet weather station (Indiana, USA). Image courtesy of Purdue University.

4 Implementation in the IFS

4.1 Astronomy

The prediction of solar eclipses requires accurate calculations of the positions of Sun and Moon relative to Earth. Since an accuracy of a few kilometres should be sufficient for all IFS applications, the choice was made to use:

- the VSOP87D solutions proposed by Bretagnon and Francou (1988) for Sun's position;
- the ELP-MPP02 solutions of Chapront and Francou (2003) for Moon's position;
- formulas for Dynamical Time and Greenwich Mean Sidereal Time definition, nutation corrections in longitude and obliquity, and aberration correction from Meeus (1998);
- formulas for ΔT (namely the difference between Dynamical Time and Universal Time) from NASA (see https://eclipse.gsfc.nasa.gov/SEcat5/deltatpoly.html);

- the GRS80 ellipsoid, to account for the impact of Earth's polar flattening.

The VSOP87D and ELP-MPP02 solutions only rely on a few external ASCII data files, which contain all coefficients required to calculate orbital positions for the selected date and time. One should note that only dates after 1900 are considered in the current IFS implementation of solar eclipses, since it was deemed unlikely that any reanalysis would ever be performed prior to that year. However, if needed, the latter limitation could be easily alleviated by implementing the appropriate formulas for ΔT for the desired period. One should also stress that the accuracy of eclipse predictions is expected to degrade for dates several centuries into the future, partly because of the impact of accumulated uncertainties in Earth's rotation on the evolution of ΔT.

Figure 3 displays various statistics (mean, standard deviation, 5% and 95% quantiles) for the error of the umbra's central location predicted by IFS relative to NASA's reference path. Statistics include all 132 total eclipses of the period 1900 to 2100 and are stratified against solar elevation. Besides, IFS and NASA's eclipse paths are compared every 2 minutes, from the beginning to the end of each eclipse. The additional purple curve in Fig.3, which shows the population in each 3° bin of solar elevation, indicates that the majority of cases involved in the statistics have solar elevations between 15° and 75°. For solar elevations above 20°, the mean and standard deviation errors are a few kilometres at most. The larger errors for solar elevations below 10° are likely due to the associated stretching of the eclipse's umbra on Earth's surface; in such cases, even tiny errors in the lunar or solar angular positions may translate into larger positional errors; however, one should stress that when the sun is very low over the horizon, the radiative (and meteorological) impact of the eclipse will be negligible. Therefore, the level of accuracy of the proposed IFS eclipse path computations is deemed sufficient for all currently envisaged applications.

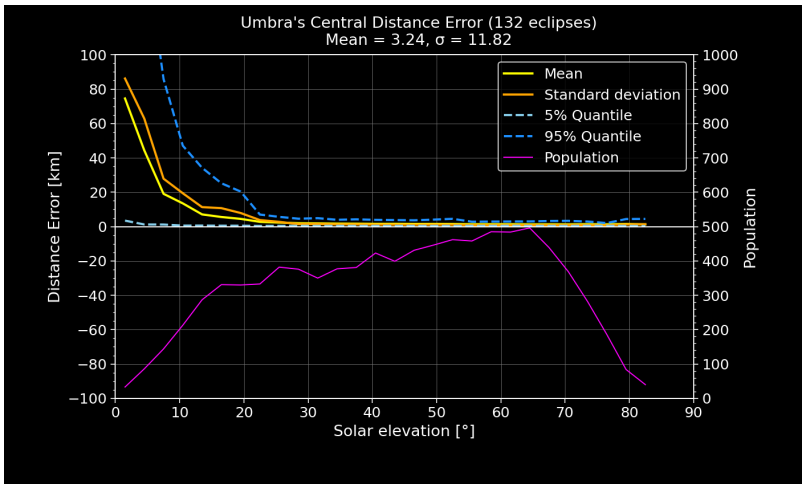

Figure 3: Error statistics for the umbra's central location (in km) predicted by IFS with respect to NASA's reference path: mean (solid yellow line), standard deviation (solid orange line), 5% quantile (dashed cyan line) and 95% quantile (dashed blue line). Statistics include all 132 total solar eclipses between 1900 and 2100, and are binned according to solar elevation (x-axis). Population in each solar elevation bin is displayed with the purple line (labels along the right y-axis).

Once the eclipse path has been calculated, the fractional area of Sun's disc eclipsed by the Moon, f_{eclip},

is computed as

$$f_{eclip} = \begin{cases} 1 & \text{if } \tau \leq \varepsilon_M - \varepsilon_S \\ \frac{1}{\pi\varepsilon_S^2}\Big(\varepsilon_S^2 \arccos\big(\frac{\tau^2+\varepsilon_S^2-\varepsilon_M^2}{2\tau\varepsilon_S}\big) + \varepsilon_M^2 \arccos\big(\frac{\tau^2+\varepsilon_M^2-\varepsilon_S^2}{2\tau\varepsilon_M}\big)\ldots \\ -0.5\sqrt{(\varepsilon_S+\varepsilon_M-\tau)(\tau+\varepsilon_S-\varepsilon_M)(\tau-\varepsilon_S+\varepsilon_M)(\tau+\varepsilon_S+\varepsilon_M)}\Big) & \text{if } \tau > \varepsilon_M - \varepsilon_S \text{ and } \tau < \varepsilon_M + \varepsilon_S \\ \frac{\varepsilon_M}{\varepsilon_S}^2 & \text{if } \tau \leq \varepsilon_S - \varepsilon_M \\ 0 & \text{otherwise} \end{cases} \tag{1}$$

where ε_M and ε_S respectively denote the angular sizes of the Moon and the Sun as viewed from the selected location on Earth, at the selected time; τ is the angular distance between the centres of the lunar and solar discs. Note that the first, second and third cases in Equation (1) correspond to the phase of totality, the partial phase, and the annular phase, respectively. The geographically and time dependent fraction f_{eclip} varies between 0 (no eclipse) and 1 (total eclipse). The impact of the eclipse is taken into account by simply multiplying the incoming solar flux at the top of the atmosphere by f_{eclip}, at each time step of the IFS forecast. All meteorological impacts of a given eclipse in the IFS will stem from this modulation of the incoming solar flux.

One should note the following simplifications or possible sources of uncertainty in the current implementation of solar eclipses (even though their impact in the IFS is expected to be very small):

- Solar limb's darkening is currently ignored (mainly relevant near totality);
- Lunar limb's irregularities due to the combination of lunar orography, librations and flattening are not considered (complicated);
- The influence of observer's altitude on Earth is neglected;
- Our knowledge of the solar disc's size and shape is slightly uncertain.

As a final remark, the additional computational cost of solar eclipses is negligible, since no 3D quantities are involved, unlike in IFS dynamical and physical calculations.

4.2 IFS code changes

The following IFS routines have been either added or modified (from IFS version 49R2 onwards):

- **yomastro.F90** (new): Declarations of astronomy-related quantities and subroutines for reading VSOP87D and ELP-MPP02 coefficient files;
- **func_astro.F90** (new): Some ancillary functions for geographic to cartesian coordinates conversion;
- **compute_astronomy.F90**: Computation of the positions of the Moon and Sun relative to Earth at a given model time step;
- **solar_eclipse.F90** (new): Computation of the corresponding fraction of the Sun eclipsed by the Moon at each model grid point.
- **radheatn.F90**: Now includes the scaling of the incoming solar flux at the top of the atmosphere by the eclipsed solar fraction.

The new switch **LSOLAR_ECLIPSES** in namelist **NAEPHY** should be set to true to activate solar eclipse computations in both forecasts and data assimilation.

5 Impact on forecasts

To evaluate the impact of the inclusion of solar eclipses in IFS forecasts, two 24-hour range simulations, with and without eclipses respectively, were run on 8 April 2024, when a total solar eclipse travelled from the Central Pacific to North America (starting at 1542 UTC), before vanishing over the North Atlantic (at 2052 UTC). In the rest of this report, the two IFS experiments will be referred to as **FC_ECLIPSE** and **FC_NO_ECLIPSE**, respectively. Figure 4 depicts the whole eclipse path calculated by the IFS. As expected, the umbra's central locations from the IFS (f_{eclip} = 1) agree very well with NASA's reference positions (white dots).

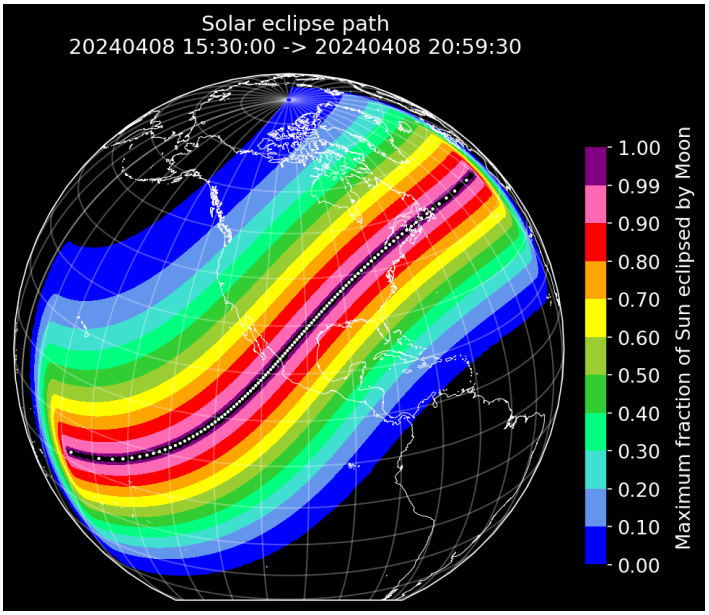

Figure 4: Path of the total solar eclipse of 8 April 2024. Colour shading shows the fraction of the Sun eclipsed by the Moon (f_{eclip}) as predicted by the IFS, while small white dots correspond to the reference central path (2-min interval) computed by Fred Espenak (NASA/GSFC).

The two weather forecasts were run using ECMWF's current operational spectral truncation of TCo1279 (i.e., 9-km resolution) and 137 vertical levels, and were started at 0000 UTC on 8 April 2024. In contrast to the operational configuration, the model time step was set to 2 min (instead of 7.5 min) and the radiation scheme was called at every model time step (instead of hourly) and on the full model grid (rather than on the TCo399 grid). This special set-up was chosen to ensure a good representation of the fast changes in radiation that occur during an eclipse. However, section 5.2.8 will demonstrate that the meteorological impacts in the forecast remain comparable when using much coarser resolutions, longer time steps, and the standard reduced set-up for radiative computations.

5.1 Background meteorology

Figure 5 displays the general meteorological situation over North America on 8 April 2024 1900 UTC, when the lunar umbra is centered at 37.33°N and 89.78°W. The low (resp. high) values of 500 hPa geopotential height over the northwest of the domain (resp. over the Caribbean) imply a widespread mid-tropospheric southwesterly flow over the Central USA. Clear-sky conditions dominates over southern

Mexico and the extreme west and southwest of the USA, while cloudy (convective) systems affects parts of the southern USA (e.g., Texas). Mostly fair weather conditions occur south of the Great Lakes, especially over Indiana. The full impact of the eclipse is therefore expected to be observed at the Purdue Mesonet stations (see section 3.2) used in this study.

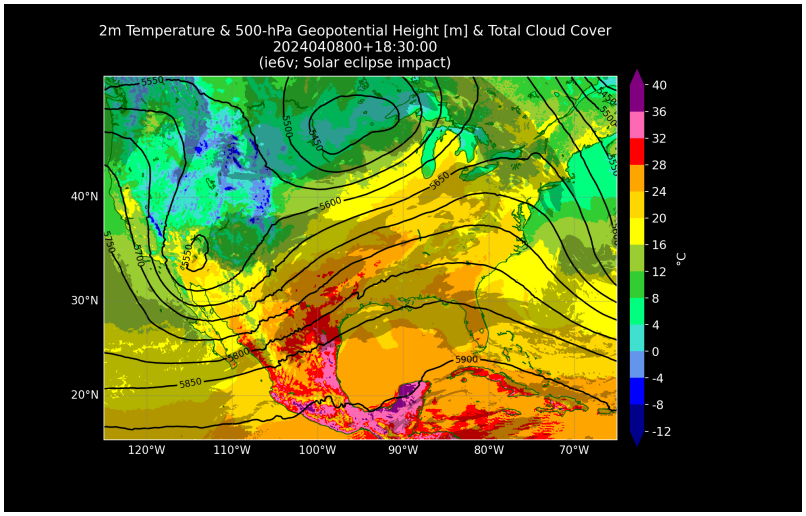

Figure 5: Overview of the meteorological situation over North America on 8 April 2024 1900 UTC (from an IFS 19h range 9-km forecast): 2-m temperature (colour shading; in °C), 500-hPa geopotential (black isolines; in metres), total cloud cover above 0.8 (grey shading). At that time, the total eclipse is centered at 37.33°N and 89.78°W.

An additional overview of meteorological conditions on 8 April 2024 at 1830 UTC over the Americas is presented in Fig.6. This figure compares a natural colour composite image from ABI[3] on board NOAA's[4] GOES-16[5] satellite with a corresponding simulated image from the IFS. The latter image was obtained by running the radiative transfer software RTTOV (Radiative Transfer for TOVS; Saunders *et al.*, 2018) combined with MFASIS (Method for FAst Satellite Image Synthesis; Scheck *et al.*, 2016) on output fields from FC_ECLIPSE (more details on this technique in Lopez and Matricardi, 2022). Figure 6 highlights the overall good agreement between simulation and observations, both in terms of the cloud cover over North America and of the eclipse itself.

5.2 Impact of eclipse on predicted meteorological variables and validation

First, Fig.7 displays the locations of the three Purdue Mesonet stations (labelled S, A, and D) used for forecast validation, relative to the eclipse path. This figure indicates that the eclipse is total at stations S and D, but only partial at station A ($f_{eclip} \approx 0.973$). Also note that original 3-sec observations have been averaged to 2-min time intervals before any validation, to match the time step used in the IFS simulations.

[3] Advanced Baseline Imager
[4] National Oceanic and Atmospheric Administration, USA
[5] Geostationary Operational Environmental Satellite

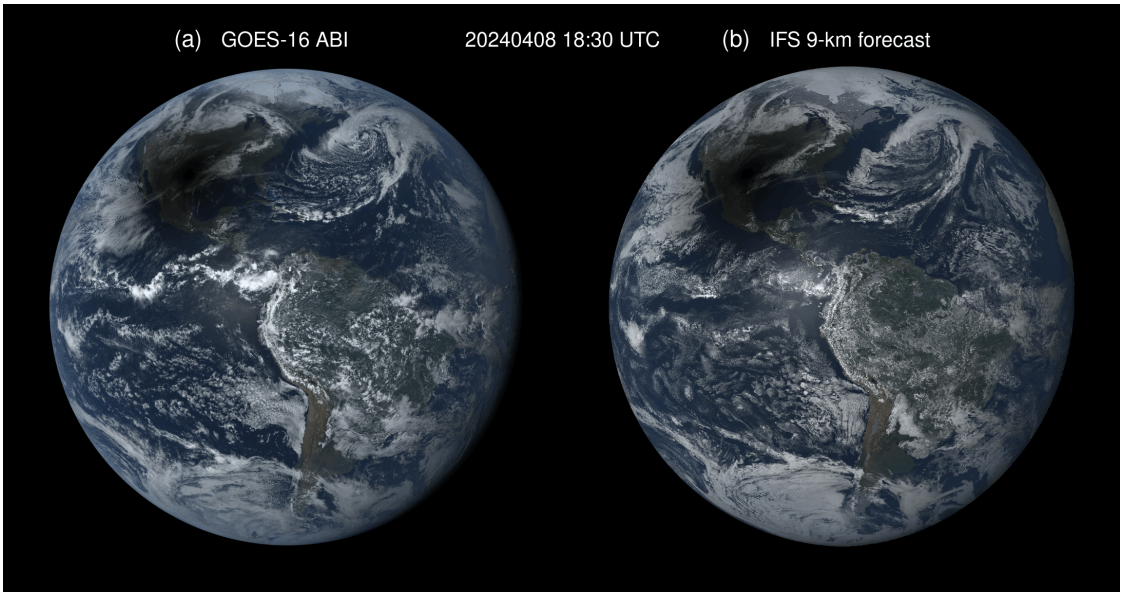

Figure 6: Comparison of two natural colour satellite images on 8 April 2024 at 1830 UTC: (a) observed by NOAA GOES-16 ABI and (b) simulated by running RTTOV/MFASIS on output fields from FC_ECLIPSE.

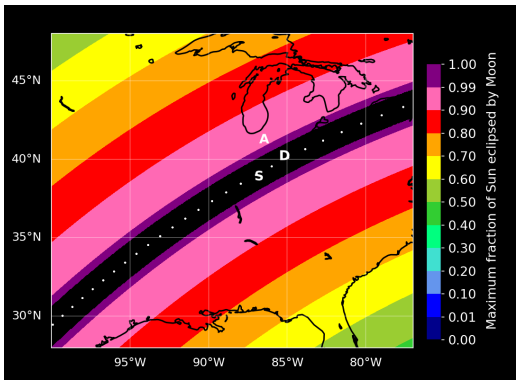

Figure 7: Map showing the locations of the three Purdue Mesonet weather stations (labelled S, A, D) used in this study, as well as the eclipse path predicted by IFS within the subdomain (colour shading; totality in black). White dots show the reference track from Fred Espenak (NASA/GSFC).

5.2.1 Solar flux

As a preliminary validation of the IFS forecast, Fig.8 displays the evolution of the surface solar flux predicted by FC_ECLIPSE and FC_NO_ECLIPSE against measurements at Purdue stations S and A (panels (a) and (b), respectively). At both stations, the maximum eclipse is observed and simulated a few minutes after 1900 UTC. The agreement between simulation (dashed curve) and observations (solid curve) in each panel confirms that the eclipse's location and timing are accurately predicted by the IFS. At station S, Fig.8a indicates that the solar flux vanishes completely in both FC_ECLIPSE and observations. One should note that the underestimation by around 100 W m^{-2} in the forecasts before the eclipse in Fig.8a is caused by a slight overestimation of high cloud cover in the IFS (not shown). Besides, the high-frequency fluctuations of the observed solar flux (especially before the eclipse) in Fig.8a,b are likely due

to variations in the thickness of the high clouds present on that day. The curves for the forecasts look much smoother, mainly because of the 9-km resolution used in the simulations, which limits the ability of the model to represent very small-scale variations realistically. At station A, where the eclipse is only partial, Fig.8b shows that the solar flux in FC_ECLIPSE drops to about 12 W m^{-2}, consistent with the observations.

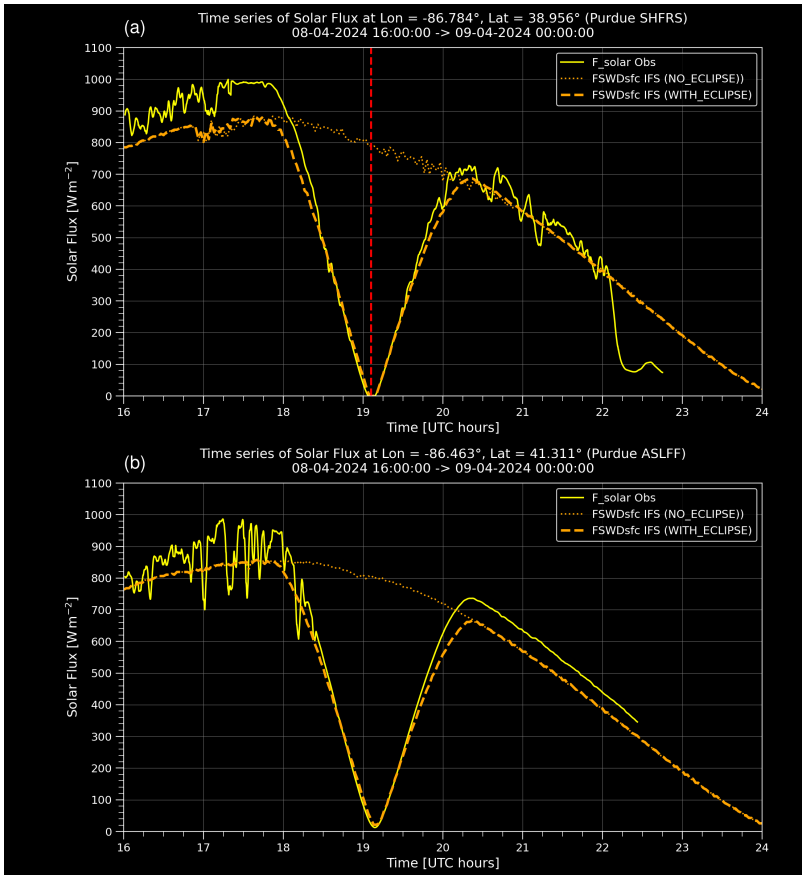

Figure 8: Evolution of the surface solar flux (in W m^{-2}) from FC_ECLIPSE (dashed orange line) and FC_NO_ECLIPSE (dotted orange line), as well as observed (solid yellow line) at Purdue Mesonet stations S (panel (a); total eclipse) and A (panel (b); 97.3% partial eclipse). The vertical dashed red line indicates the time of the total eclipse maximum at station S. The displayed period runs from 8 April 2024 1600 UTC to 9 April 2024 0000 UTC, i.e., for forecast ranges between +16h and +24h. Note that local solar noon roughly corresponds to 1750 UTC.

5.2.2 *Temperature*

Figure 9 clearly illustrates the significant drop in 2-m temperature (T_{2m}) over land (down to $-6°$C, right after eclipse maximum in panel (a)) in FC_ECLIPSE relative to FC_NO_ECLIPSE. This low-level cooling is mainly due to the drop in incoming solar radiation that was illustrated in Fig.8. The influence of the eclipse on low-level meteorology is negligible over water bodies (oceans and lakes) because of the much larger thermal inertia of water. Note that the small noise visible over sea in the vicinity of steep orography (e.g., off the Pacific coast of Mexico) should be disregarded here, since it is due to the Gibbs phenomenon when using a spectral model in regions with sharp gradients. Figure 9a also shows that

the impact of the eclipse on the forecast affects a large part of North America (i.e., the eclipse's entire penumbra; colour shaded in Fig.4), not just the 180-km wide path of totality. Figure 9b highlights that a cooling down to $-2°$C persists over most of the domain in FC_ECLIPSE, even several hours after the eclipse has vanished over the North Atlantic. Note that an animation of the impact over the entire period of the eclipse is available in section "Supplementary material" at the end of this document.

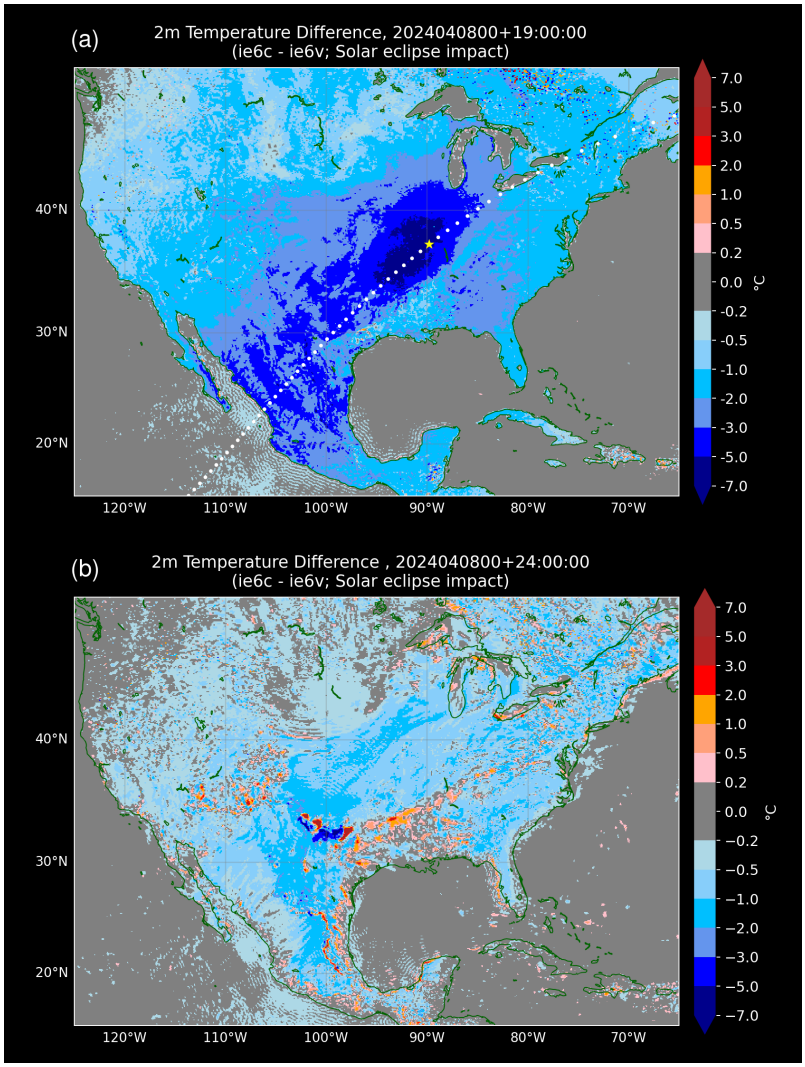

Figure 9: Maps of 2-m temperature differences (in °C) between FC_ECLIPSE and FC_NO_ECLIPSE on (a) 8 April 2024 at 1900 UTC and (b) 9 April 2024 at 0000 UTC (19h and 24h range forecast, respectively). Blue (resp. red) shading indicates a cooling (resp. warming) in FC_ECLIPSE relative to FC_NO_ECLIPSE. On panel (a), the path of the total eclipse is shown with white dots, while the yellow star marks its position at 1900 UTC. In panel (b), 3 hours have passed since the eclipse ended over the North Atlantic.

Figure 10 displays the evolution of air temperature at various heights very near the surface, at Purdue Mesonet stations S and D. First, one should note that the cold bias in 2-m temperature in the forecast in panel (a) ($\approx -2.5°$C) is likely due to a slight overestimation of high cloud cover in the model, consistent with the solar flux bias previously identified in Fig.8a. As expected, the sharp drop in low-level temperature caused by the total eclipse is strongest at the surface, and gradually decreases in magnitude with height, in both forecast (dashed lines) and observations (solid lines). Skin temperature (T_{skin}; dashed

light green curve) in forecast FC_ECLIPSE falls by more than 10°C at both stations, and the temperature minimum is predicted to occur just a couple of minutes after the total eclipse maximum. While the latter timing can be explained by the fast response of ground temperatures to variations in incident solar radiation, the predicted T_{2m} (cyan dashed curve) reaches its minimum 15 to 25 min too early compared to observations (cyan solid curve), especially at station S (panel (a)). In addition, the dip in T_{2m} is overestimated by a couple of degrees Celsius in FC_ECLIPSE. These last two discrepancies suggest that, in the fast-changing context of the solar eclipse, too much weight might be given to T_{skin} in the forecast model's T_{2m} diagnostic. The latter is obtained via an interpolation of the assumed logarithmic temperature profile between T_{skin} and temperature at the lowest model level (T_{ml137}; at roughly 10-m height; dashed magenta curve in Fig.10).

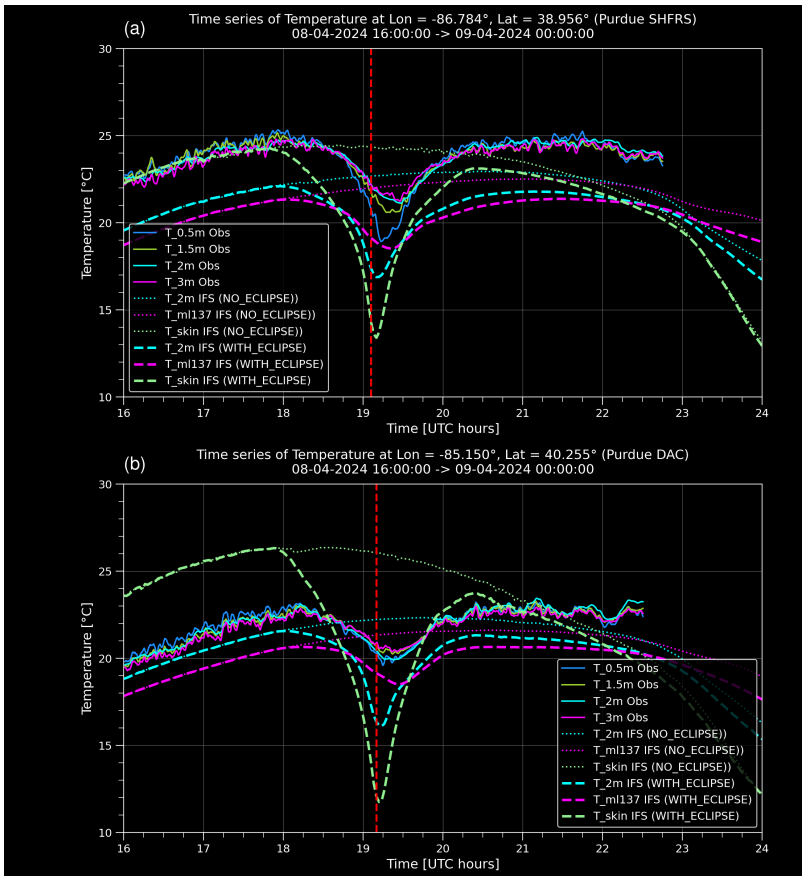

Figure 10: Evolution of air temperature at various heights near the surface (in °C) from FC_ECLIPSE (dashed lines) and FC_NO_ECLIPSE (dotted lines), as well as observed (solid lines) at Purdue Mesonet stations S (panel (a)) and D (panel (b)). Observations are shown at 0.5, 1.5, 2 and 3-m heights, while forecast skin temperature, temperature at 2 m and at the lowest model level (number 137; ≈ 10-m height) are also displayed (see plot's legend for colours). Layout and valid period are similar to Fig.8.

5.2.3 Boundary layer height

As a result of the quick and strong response of land surfaces to changes in incoming solar radiation, the response of the atmosphere is expected to be particularly pronounced inside the well-mixed daytime boundary layer, which would typically extend up to a couple of kilometres above the surface in normal

fair-weather mid-day conditions. Figure 11 compares the diagnosed boundary layer top heights (BLH) from FC_NO_ECLIPSE and FC_ECLIPSE on 8 April 2024 at 1900 UTC. Figure 11c shows that BLH undergoes a significant drop over most land regions inside the plotted domain when the forecast accounts for the eclipse. This drop is particularly large in regions with fair weather. Over the central USA in particular, BLH decreases by over 1 km, leaving a boundary layer hardly 150-m thick in Fig.11b. The reduction of BLH has a similar magnitude over the clear-sky regions of southwestern USA and Mexico, where BLH values would otherwise typically range between 2 and 4 km (Fig.11a). An animation of the eclipse impact on BLH in the forecasts shows that the region of maximum impact on BLH closely follows the path of the eclipse maximum, with a time lag of just a few minutes (see section "Supplementary material"). It is worth mentioning that for the same eclipse, Pasken *et al.* (2024) reported a drop of around 500 m in the capping inversion 30 minutes after totality in fair-weather conditions over Missouri (USA), from dedicated radiosonde flights.

5.2.4 *Vertical distribution of temperature*

To document the temporal evolution of the typical eclipse's impact on the temperature forecast throughout the vertical, Fig.12 displays a Hovmöller diagram of FC_NO_ECLIPSE−FC_ECLIPSE differences over Purdue Mesonet station S. The strong gradual cooling inside the boundary layer and the collapse of the latter are both very clear. A more moderate cooling (down to -2°C) also appears at upper atmospheric levels, as a result of the direct interaction of the ozone layer with solar radiation (partially accounted for in IFS). This particular impact will be confirmed as an improvement in the context of data assimilation, in section 6. Finally, the thin layer with a heating signal just above the cooled boundary layer is due to the development of local subsidence, which leads to the creation of an inversion layer in FC_ECLIPSE (as suggested by the tephigrams shown in Fig.13).

5.2.5 *Dew point temperature*

Figure 14 highlights the significant increase in 2-m dew point temperature (T_{d_2m}) over a large part of North America (up to 6°C) in FC_ECLIPSE relative to FC_NO_ECLIPSE, with a typical delay of 30 minutes after eclipse maximum. Note that Fig.14 is valid half an hour after Fig.9. The corresponding moistening is particularly pronounced over cloud-free regions south of the Great Lakes and over Mexico (see Fig.5). In contrast, a relative cooling in T_{d_2m} (i.e., drying) is generally found in cloudy regions, although with a much smaller magnitude ($< 1^{\circ}$C). Figure 15 depicts the evolution of 2-m dew point temperature at Purdue Mesonet station S. First, the rather large positive bias ($\approx 5^{\circ}$C) in FC_ECLIPSE can be explained by the fact that station S is located at the edge of a slightly misplaced low-level intrusion of moist air from the southwest (not shown). Despite that, and in contrast to FC_NO_ECLIPSE, the evolution from FC_ECLIPSE agrees quite well with observations, with a decrease of T_{d_2m} (= drying) before the beginning of the partial eclipse (1800 UTC), followed by an increase in T_{d_2m} (= moistening) starting just before eclipse maximum. The amplitude of both the drying and moistening phases is more pronounced in the observations ($\approx 7^{\circ}$C) than in FC_ECLIPSE ($\approx 3.5^{\circ}$C).

An explanation for the low-level moistening found in Fig.14, Fig.15 and Fig.13 around the eclipse maximum can be formulated by comparing the evolution of several output fields from FC_ECLIPSE at Purdue station S in Fig.16. Note that the evolution of T_{d_2m} (dark blue curve) was already plotted in Fig.15. Figure 16 highlights a crucial difference between the evolution of surface evaporation (cyan curve) and that of BLH (magenta curve). On the one hand, surface evaporation quickly recovers after eclipse maximum, as it appears to be mainly driven by the solar flux (orange curve). This is expected given the cloud-free

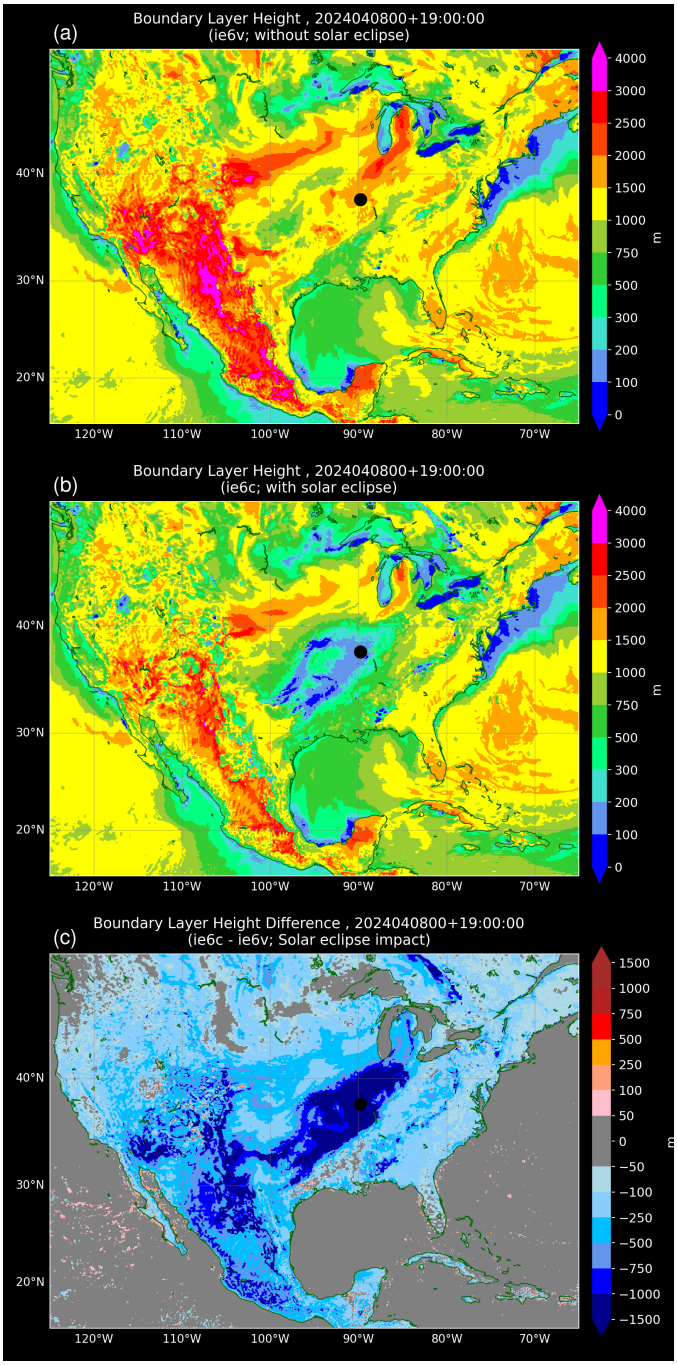

Figure 11: Maps of IFS diagnostic boundary layer heights (in m) on 8 April 2024 at 1900 UTC from (a) FC_NO_ECLIPSE and (b) FC_ECLIPSE, and (c) the difference FC_ECLIPSE−FC_NO_ECLIPSE. The black dot on each panel pinpoints the total eclipse region at 1900 UTC.

stable conditions that prevail at station S. On the other hand, BLH takes more than 2 hours to recover from its earlier spectacular collapse. This implies that during the two hours following the eclipse maximum, there is intense evaporation from the surface into a still very shallow boundary layer, which can only lead to an increase in specific humidity (hence the increase in T_{d_2m}). Last, but not least, the much lower dew point temperatures inside the 790-900 hPa layer in FC_ECLIPSE in Fig.13 indicate that, in

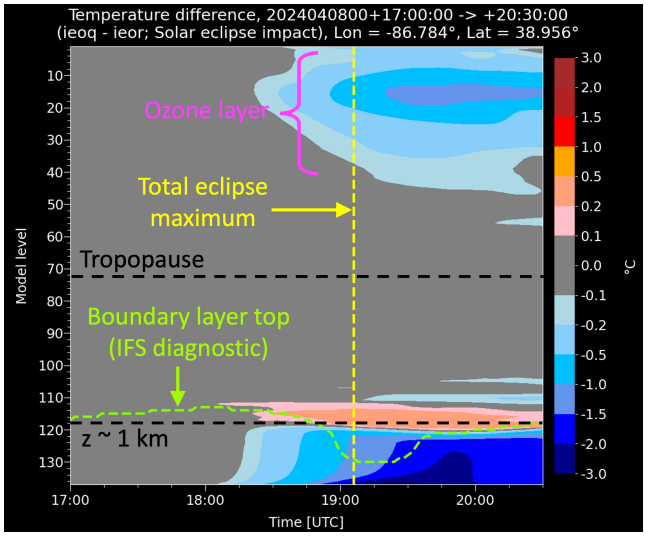

Figure 12: Hovmöller diagram of the temperature differences (in °C) between FC_ECLIPSE and FC_NO_ECLIPSE at Purdue Mesonet station S. UTC time is shown along the x-axis, while the y-axis corresponds to vertical model levels (level 1 ≈ 80-km altitude; level 137 ≈ 10-m height). Blue (resp. red) shading indicates a relative cooling (resp. warming) in FC_ECLIPSE relative to FC_NO_ECLIPSE. The light green dashed curve denotes the boundary layer top height (IFS diagnostic), while the two horizontal black dashed lines roughly indicate the 1-km and tropopause levels. The approximate extent of the upper-atmospheric ozone layer is drawn in magenta.

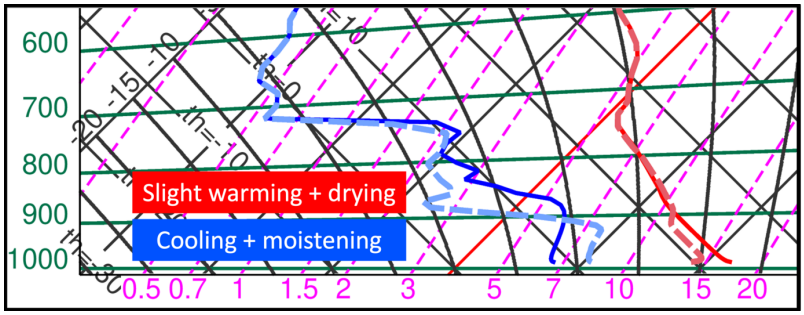

Figure 13: Tephigrams based on model level data from FC_ECLIPSE (dashed lines) and FC_NO_ECLIPSE (solid lines), valid on 8 April 2024 at 1916 UTC. Red (resp. blue) curves show the respective dry (dew point) temperature profiles between the surface and roughly 5-km altitude. Pressure labels (hPa) are shown along the y-axis, while the usual slantwise dry isotherms are plotted every 10°C (red solid line for 0°C; black solid otherwise). Magenta dashed lines and labels along the x-axis show saturation mixing ratios (g kg^{-1}).

parallel to the intense low-level moistening, the inclusion of the eclipse in the model brings a significant drying above the collapsed boundary layer (through dry air subsidence).

5.2.6 *Wind speed*

Besides its pronounced impact on low-level temperature and moisture, the inclusion of the eclipse in the forecast yields a widespread reduction in 10-m wind speed over land, as illustrated in Fig.17c, with a drop of up to -3 m s^{-1} along the path of totality. Such response can be explained by the cooling and hence stabilization of the boundary layer, as already evidenced in Fig.12. In some clear-sky regions

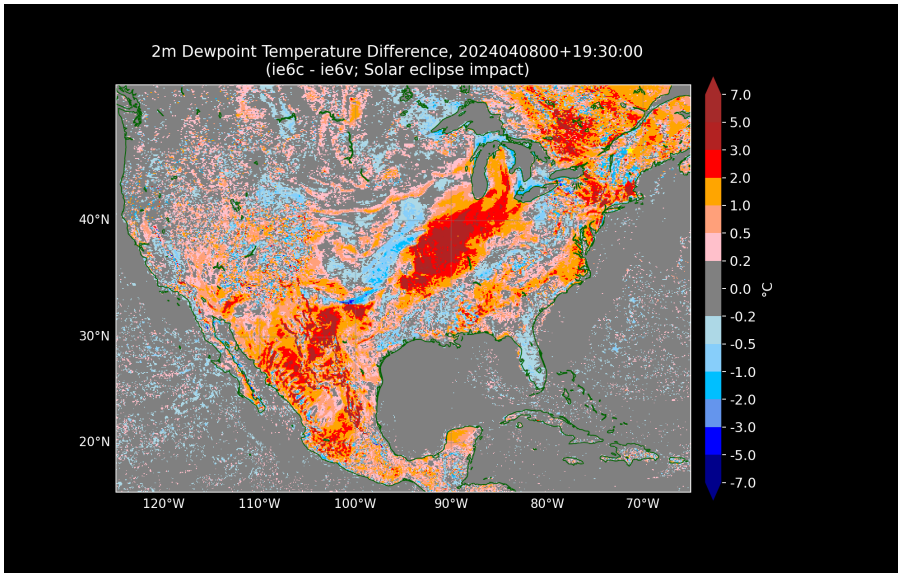

Figure 14: Map of 2-m dew point temperature differences (in °C) between FC_ECLIPSE and FC_NO_ECLIPSE on 8 April 2024 at 1930 UTC (19.5h range forecast). Blue (resp. red) shading indicates a relative cooling (resp. warming) in FC_ECLIPSE relative to FC_NO_ECLIPSE, which corresponds to a drying (resp. moistening). The yellow star marks the total eclipse position at 1930 UTC, over Maine, USA.

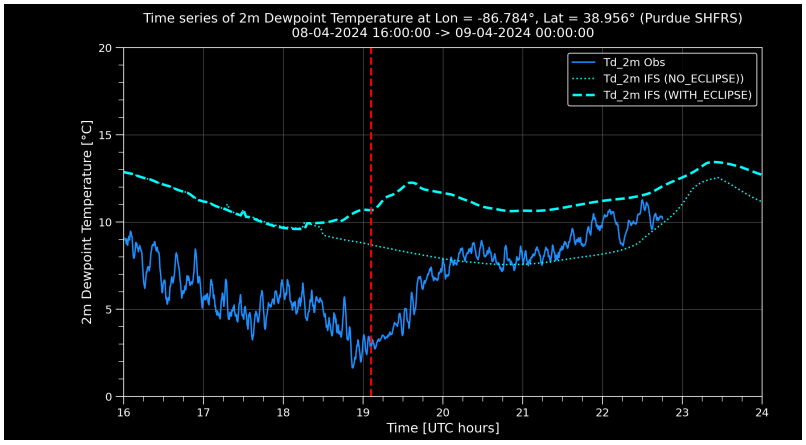

Figure 15: Evolution of 2-m dew point temperature (in °C) from FC_ECLIPSE (dashed cyan line) and FC_NO_ECLIPSE (dotted cyan line), as well as observed (solid blue line) at Purdue Mesonet station S. Layout and valid period are similar to Fig.8.

of the central USA, Fig.17b suggests that the 10-m wind speed in FC_ECLIPSE drops to almost zero around eclipse maximum. In contrast to temperature, during the hours after the eclipse, the impact on the predicted 10-m wind speed tends to become more variable (see animation in section "Supplementary material"). For instance, after 2000 UTC, the wind seems to pick up in FC_ECLIPSE over regions of the central USA that had been affected by the strongest wind speed reductions one hour earlier, in Fig.17c. This could be due to the quick reactivation of turbulence as soon as solar radiation recovers after the eclipse, even though the atmosphere in FC_ECLIPSE remains cooler than in FC_NO_ECLIPSE.

In Fig.18, the evolution of simulated low-level wind speeds is compared with measurements at Purdue

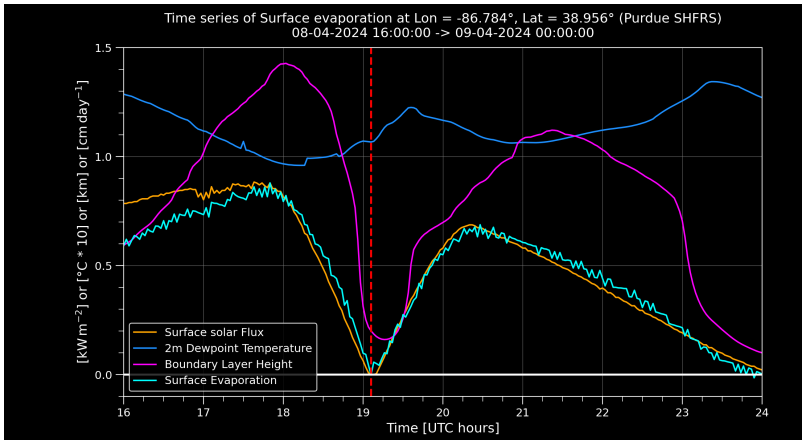

Figure 16: Evolution of various quantities from forecast FC_ECLIPSE at the location of Purdue Mesonet station S: 2-m dew point temperature (blue line), surface solar flux (orange line), boundary layer height (magenta line), and surface evaporation (cyan line). Respective units are indicated in the title of the y-axis (with some scaling, for plotting convenience). Layout and valid period as in Fig.8.

Mesonet station D. As already underlined, the smoother curves for the forecasts compared to observations are mainly due to the limited 9-km resolution of the simulations. Fig.18 exhibits a substantial drop in wind speed in both observations and FC_ECLIPSE. Here, one should keep in mind that observations are collected at a 3-m height, while the two types of low-level wind speed displayed from the forecasts are valid at 10 m (diagnostic) and at the model's bottom level (also situated at around 10-m height). The stronger surface drag at lower heights might explain why the drop in wind speed is around -3.0 m s^{-1} in the measurements, but only -1.8 m s^{-1} in the model. The origin of the wave-like patterns found in the two model curves around the maximum of the eclipse is uncertain.

5.2.7 *Other variables*

Unlike temperature, humidity and wind, simulated clouds and precipitation do not exhibit any clear, widespread impact from the eclipse, when comparing FC_ECLIPSE with FC_NO_ECLIPSE (not shown). Only a reduction in upper-tropospheric cloud cover around the time of maximum eclipse can be identified over fair-weather regions of the central USA. Elsewhere, changes in clouds and precipitation, albeit not necessarily small, do not present any pattern easily attributable to the eclipse. As far as mean-sea-level pressure is concerned, the only noticeable feature is a slight increase (less than 2.5 hPa) in FC_ECLIPSE in the lee of the Sierra Madre in Mexico, which persists until nighttime (see animation in section "Supplementary material"). This might be the result of the local low-level cooling and enhanced atmospheric subsidence caused by the eclipse.

5.2.8 *Sensitivity of impact to model's set-up*

To assess the sensitivity of the eclipse's impact to the model's time step (Δt), horizontal resolution (Δx) and radiation configuration, additional forecasts were run using different values of these parameters (all started on 8 April 2024 0000 UTC). As for radiation, two configurations have been tested: the "full" one (FULL_RAD: full radiation called at every time step and each model grid point) and the cheaper operational one (OPER_RAD: full radiation called every hour and on a coarser TCo399 grid). It is worth

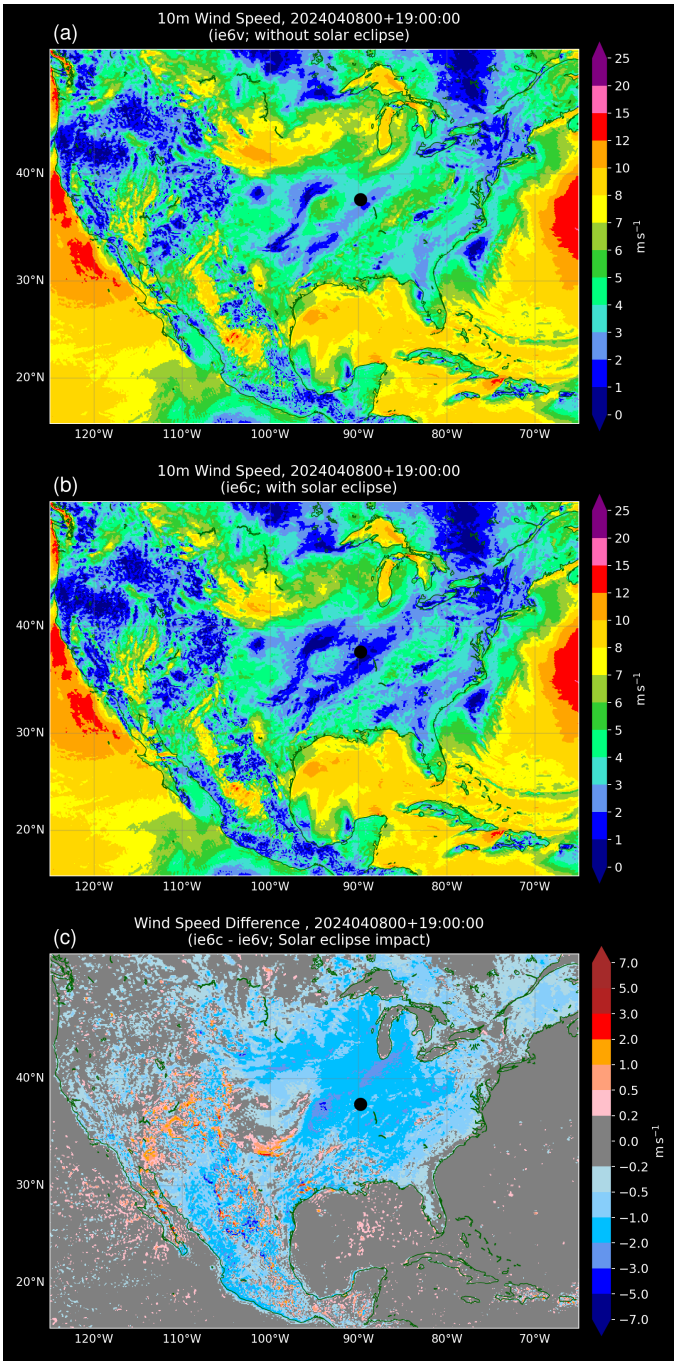

Figure 17: Same as in Fig.11, but for 10-m wind speed (in m s^{-1}).

stressing that in the OPER_RAD configuration, variations in local solar angle and surface temperature between model time steps are allowed to change radiative fluxes, but cloud radiative effects are only refreshed every hour. Figure 19 compares the FC_ECLIPSE−FC_NO_ECLIPSE impacts on T_{2m} (19h-range forecasts) for four different simulation set-ups: (a) $\Delta x = 9$ km, $\Delta t = 2$ min, FULL_RAD; (b) $\Delta x = 9$ km, $\Delta t = 7.5$ min, OPER_RAD; (c) $\Delta x = 18$ km, $\Delta t = 12$ min OPER_RAD; (d) $\Delta x = 28$ km, $\Delta t = 15$ min, OPER_RAD. Figure 19 confirms that the impact of the eclipse on the forecast does not

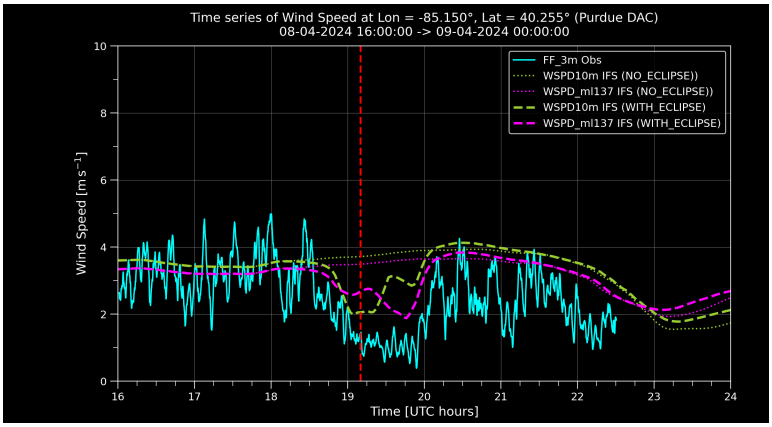

Figure 18: Evolution of low-level wind speed (in m s^{-1}) from FC_ECLIPSE (dashed lines) and FC_NO_ECLIPSE (dotted lines), as well as observed (solid cyan line) at Purdue Mesonet station D. From the forecasts, the curves for both the IFS diagnostic 10-m wind speed (light green) and wind speed on the model's bottom level 137 (magenta) are displayed. Observed wind speed is measured at a 3-m height. Layout and valid period as in Fig.8.

depend too much on model resolution, time step or configuration of the radiation computations, at least within the scope of ECMWF applications. Only the maximum impact near the path of totality is slightly reduced at coarser resolution, which is easily understandable. This suggests that we can expect the effect of eclipses to be properly represented in the next ECMWF global reanalysis (ERA6), with its planned resolution of 14 km.

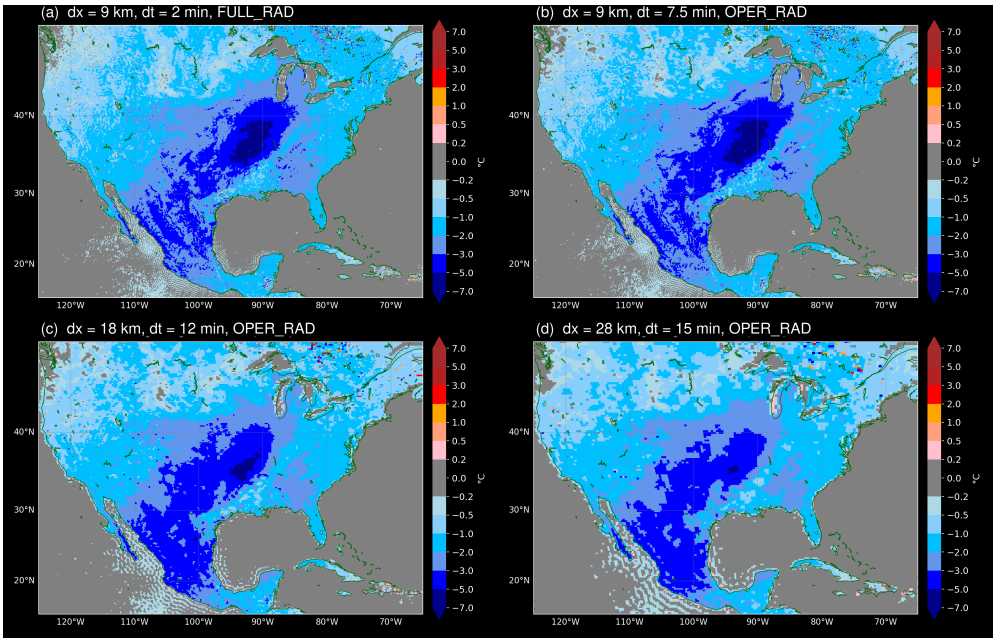

Figure 19: Eclipse impact on T_{2m} forecast (in °C) over North America for four different combinations of horizontal resolution, time step and radiation configuration, as indicated above each panel. The valid date is 8 April 2024 1900 UTC and impacts are based on 19h-range forecasts.

6 Impact on data assimilation

One of the main goals of data assimilation is to generate optimal 3D representations of weather and surface conditions (or analyses) that can be used to initialize numerical weather forecasts. In the 4D-Var method used at ECMWF (see section 2), the forecast model is involved both in the generation of the background state and in the minimizations, since the model state needs to be calculated at the exact time of each observation (so that observation−model departures can be computed). Given the significant meteorological impacts found throughout section 5, neglecting the occurrence of a solar eclipse in the data assimilation process is likely to lead to significant unwanted errors in both model background and 4D-Var minimizations. Solar eclipse computations have therefore also been implemented in the tangent-linear and adjoint versions of the forecast model, which play a central role in 4D-Var minimizations.

The impact of including solar eclipses on the performance of data assimilation is assessed by comparing two 4D-Var single-cycle experiments with the IFS, one with, the other without solar eclipse. These experiments will be hereafter referred to as 4DVAR_ECLIPSE and 4DVAR_NO_ECLIPSE, respectively. The selected 4D-Var cycle date is 8 April 2024 at 1200 UTC, using all operational observations between 0900 UTC and 2100 UTC, thus encompassing the entire duration of the total eclipse presented in section 5.

6.1 Background state

First, Fig.20 illustrates the impact of including the solar eclipse on the model's background state, by showing 4DVAR_ECLIPSE−4DVAR_NO_ECLIPSE differences in terms of

- Brightness temperatures simulated at observation locations for various polar-orbiting satellite instruments (IASI[6]; CrIS[7] and ATMS[8]), for channels sensitive to either upper-atmospheric (Fig.20a-c) or lower-tropospheric layers (Fig.20d);
- Simulated aircraft temperatures for flight levels between 800 and 1000 hPa (i.e., climbing and descending stages; Fig.20e).

Fig.20 clearly shows that background satellite brightness temperatures and aircraft temperatures are systematically lower when the eclipse is included, as expected. This confirms that the effect of the eclipse is properly accounted for in the calculations of the model background state.

6.2 Background and analysis departures

To go further, standard deviations (σ) of observation−analysis and observation−background departures (in terms of brightness temperatures) are displayed in Fig.21 for CrIS and ATMS channels, most of which are predominantly sensitive to temperature at various levels in the stratosphere or troposphere (see colour shading). Here, σ values for 4DVAR_ECLIPSE have been normalized by their values in 4DVAR_NO_ECLIPSE and expressed in %. Fig.21b,d clearly show that σ for background departures is usually lower when the solar eclipse is included in 4D-Var calculations. This improvement is particularly pronounced in the stratosphere (blue shading) for both CrIS and ATMS observations. Fig.21a,c suggests

[6] Infrared Atmospheric Sounding Interferometer on board EUMETSAT's MetOp satellite
[7] Cross-track Infrared Sounder on board NOAA-20, NOAA-21 & SNPP
[8] Advanced Technology Microwave Sounder on board NOAA-20, NOAA-21 & SNPP

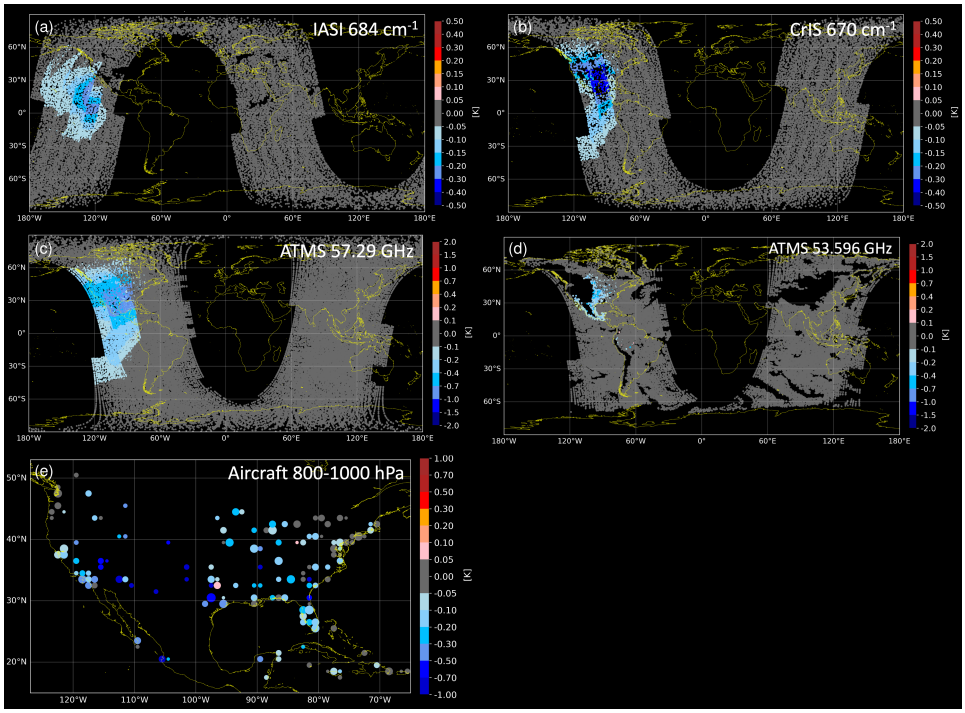

Figure 20: 4DVAR_ECLIPSE−4DVAR_NO_ECLIPSE differences in model background brightness temperatures at observation locations(in K), for various polar-orbiting satellite instruments and channels: (a) IASI 684 cm^{-1} channel; (b) CrIS 670 cm^{-1} channel; (c) ATMS 57.29 GHz channel; (d) ATMS 53.596 GHz channel. Panels (a-c) (resp. (d)) are representative of stratospheric (resp. lower-tropospheric) layers. Note that in panel (d), there are no data over higher orography (too low pressure). Panel (e) shows model background temperature differences at aircraft locations between 800 and 1000 hPa (i.e., climbing and descending stages). The valid period for all plots is 8 April 2024 between 1600 and 2100 UTC, thus encompassing the entire duration of the eclipse.

that to a lesser extent, analysis departures are also reduced in 4DVAR_ECLIPSE, which also goes in the right direction.

6.3 Number of assimilated observations

Last, but not least, Fig.22a,c reveals that the number of CrIS and AIRS[9] observations assimilated in 4D-Var increases significantly in 4DVAR_ECLIPSE compared with 4DVAR_NO_ECLIPSE, for most channels. Up to 3% (resp. 6%) more CrIS (resp. AIRS) observations are used inside the wide region affected by the eclipse, especially in channels sensitive to either stratospheric ozone or tropospheric temperature (red and green shading). More modest increases (up to 0.5%) are also found for ATMS tropospheric channels as well as IASI (not shown). This suggests that fewer observations are rejected in 4DVAR_ECLIPSE through the first-guess check, because background departures are usually smaller when the eclipse is accounted for (as previously seen in Fig.20). For observations that were not rejected in 4DVAR_NO_ECLIPSE, the Variational Quality Control (VarQC) procedure, which reduces the weight given to observations that are remote from the model background, is also expected to be less active in 4DVAR_ECLIPSE.

[9]Atmospheric Infrared Sounder on board NASA's Aqua satellite

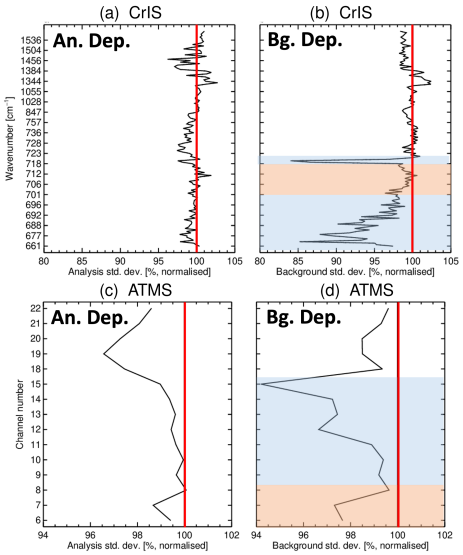

Figure 21: Standard deviation (σ) of observation−analysis (left panels) and observation−background (right panels) departures from experiment 4DVAR_ECLIPSE, for CrIS (top row) and ATMS (bottom row) channels. Black curve show σ values for 4DVAR_ECLIPSE normalized by the 4DVAR_NO_ECLIPSE value. Values below 100% indicate a reduction in σ when including the solar eclipse in 4D-Var computations, which is an improvement. Statistics are valid over the entire region affected by the eclipse (170°W/60°W and 20°S/55°N). Colour shading highlights channels' dominant sensitivity, wherever relevant (red: tropospheric temperature, blue: stratospheric temperature).

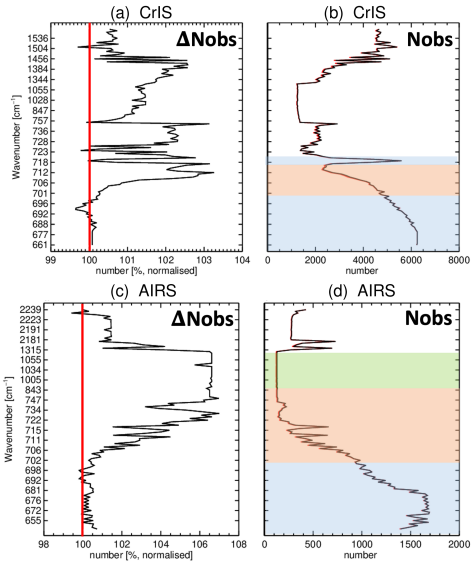

Figure 22: Impact of solar eclipse on the number of radiance observations assimilated in 4D-Var (N_{obs}) for CrIS (top row) and AIRS (bottom row) channels. Left panels: N_{obs} in 4DVAR_ECLIPSE normalized by N_{obs} in 4DVAR_NO_ECLIPSE; Right panels: Actual values of N_{obs} in 4DVAR_NO_ECLIPSE (red curve) and 4DVAR_ECLIPSE (black curve). In panels (a) and (c), values above 100% indicate an increase in N_{obs} when including the solar eclipse in 4D-Var calculations, which is an improvement. Statistics are valid over the entire region affected by the eclipse (namely 170°W/60°W and 20°S/55°N). Colour shading highlights channels' dominant sensitivity, wherever relevant (red: tropospheric temperature, blue: stratospheric temperature; green: stratospheric ozone).

7 Summary and conclusions

Solar eclipse computations have been successfully included in ECMWF's IFS, both in 4D-Var data assimilation and in numerical weather forecasts. An in-depth investigation focused on the recent total solar eclipse of 8 April 2024 over North America demonstrates that the new ability to represent the significant widespread low-level atmospheric cooling (by $-7°C$ locally), moistening (2-m dew point temperature increases by up to $6°C$) and wind speed reduction (by up to 3 m s^{-1}) caused by the eclipse, can help to make IFS predictions more realistic, as confirmed using ground-based observations. Another noticeable impact of the eclipse on the forecast is the large-scale cooling (by $-2°C$, locally) in the stratospheric ozone layer. Better forecasts of incoming solar radiation and low-level wind speeds on eclipse days are likely to become increasingly valuable to stakeholders involved in solar and wind power management (Harrison and Hanna, 2016).

In 4D-Var data assimilation, performance can be improved by including eclipses, because the model background gets closer to the observations, which results in fewer observations being rejected through quality control, over the wide region affected by the eclipse. Additional benefits can be expected once solar reflectance satellite observations start to be assimilated, since these strongly depend on incoming solar radiation. The new developments will also be helpful to better represent the 200 or so solar eclipses (of all types) that will be included in ECMWF's next reanalysis ERA6.

A more systematic evaluation of the benefits of including solar eclipses in the IFS over as many past cases as possible would be very interesting, to quantify their mean impact on forecast scores and to further understand how this impact is modulated by the presence of clouds, geographical location, season, and eclipse type.

Acknowledgements

I am very grateful to the Purdue University (Indiana, USA) for making their Mesonet station observations available at *https://ag.purdue.edu/indiana-state-climate/purdue-mesonet/2024-solar-eclipse/*, and to Fred Espenak of the National Aeronautics and Space Administration/Goddard Space Flight Center (NASA/GSFC, USA) for providing his eclipse track data at *https://eclipse.gsfc.nasa.gov/solar.html*. Special thanks also go to my ECMWF colleagues Olivier Marsden, Richard Forbes, Robin Hogan, Anton Beljaars and Mark Fielding for their help and suggestions during this work.

Supplementary material

Animations of the solar eclipse's impact (FC_ECLIPSE−FC_NO_ECLIPSE) between 8 April 2024 1550 UTC and 9 April 2024 0000 UTC (every 2 minutes) are available here, for the following parameters:
2-m Temperature
Boundary Layer Height
2-m Dew Point Temperature
Surface Evaporation
10-m Wind Speed
Total Cloud Cover
Mean-Sea-Level Pressure
Note that the loading of each animation can take a few tens of seconds.

References

Aplin, K. L., Scott, C. J. and Gray, S. L. (2016). Atmospheric changes from solar eclipses. *Phil. Trans. R. Soc. A*, **374**, doi:10.1098/rsta.2015.0217.

Bretagnon, P. and Francou, G. (1988). Astron. astrophys. *Planetary theories in rectangular and spherical variables. VSOP87 solutions*, **202**, 309–315.

Chapront, J. and Francou, G. (2003). Astron. astrophys. *The lunar theory ELP revisited: Introduction of new planetary perturbations*, **404**, 735–742.

Courtier, P., Thépaut, J.-N. and Hollingsworth, A. (1994). A strategy for operational implementation of 4D-Var using an incremental approach. *Quart. J. Roy. Meteor. Soc.*, **120**, 1367–1388.

Elmhamdi, A., Roman, M. T., Peñaloza Murillo, M. A., Pasachoff, J. M., Liu, Y., Al-Mostafa, Z. A., Maghrabi, A. H., Oloketuyi, J. and Al-Trabulsy, H. A. (2024). Impact of the Eclipsed Sun on Terrestrial Atmospheric Parameters in Desert Locations: A Comprehensive Overview and Two Events Case Study in Saudi Arabia. *Atmos.*, **15**(1), doi:10.3390/atmos15010062.

Harrison, R. and Hanna, E. (2016). The solar eclipse: a natural meteorological experiment. *Phil. Trans. R. Soc. A*, **374**, doi:10.1098/rsta.2015.0225.

Lopez, P. and Matricardi (2022). Validation of IFS+RTTOV/MFASIS 0.64-μm reflectances against observations from GOES-16, GOES-17, MSG-4 and Himawari-8. *Technical report*, ECMWF, Reading, UK, doi:10.21957/l4u0f56lm, Technical Memorandum 903, available at https://www.ecmwf.int/node/20472, 31 pages.

Meeus, J. (1998). *Astronomical Algorithms*. Willmann-Bell, Inc., Richmond, Virginia, USA, 2 edition, 477 pages.

Pasken, R., Woodford, R., Bergmann, J., Hickel, C., Ideker, M., Jackson, R., Rotter, J. and Schaefer, B. (2024). Effects of the 2024 Total Solar Eclipse on the Structure of the Planetary Boundary Layer: A Preliminary Analysis. *Atmos.*, **15**(1008), doi:10.3390/atmos15081008.

Saunders, R., Hocking, J., Turner, E., Rayer, P., Rundle, D., Brunel, P., Vidot, J., Roquet, P., Matricardi, M., Geer, A., Bormann, N. and Lupu, C. (2018). An update on the RTTOV fast radiative transfer model (currently at version 12). *Geosci. Model Dev.*, **11**, 2717–2737, doi:10.5194/gmd-11-2717-2018.

Scheck, L., Frèrebeau, P., Buras-Schnell, R. and Mayer, B. (2016). A fast radiative transfer method for the simulation of visible satellite imagery. *J. Quant. Spectrosc. Radiat. Transf.*, **175**, 54–67, doi:10.1016/j.jqsrt.2016.02.008.